DOI: 10.1002/ejic.201000599

New Oxyfluoride Pyrochlores $Li_{2-x}La_{(1+x)/3}\square_{(2x-1)/3}B_2O_6F$ (B = Nb, Ta): Average and Local Structure Characterization by XRD, TEM and ^{19}F Solid-State NMR Spectroscopy

Cyrille Galven,[a] Christophe Legein,*[a] Monique Body,[b] Jean-Louis Fourquet,[a]
Jean-Yves Buzaré,[b] Françoise Le Berre,*[a] and Marie-Pierre Crosnier-Lopez[a]

Keywords: Pyrochlores / Local structure / X-ray diffraction / NMR spectroscopy / Electron microscopy / Structure elucidation

Two new solid solutions $Li_{2-x}La_{(1+x)/3}\square_{(2x-1)/3}B_2O_6F$ (B = Ta, Nb) have been synthesized in powder form by solid-state synthesis. Their composition domain corresponds to $0.6 \le x \le 1.1$ for the Ta compounds and to $0.7 \le x \le 1.0$ for the Nb compounds. The structural study has been performed by XRD on two single crystals with the compositions $Li_{1.00}La_{0.67}\square_{0.33}Ta_2O_6F$ and $Li_{1.25}La_{0.58}\square_{0.17}Nb_2O_6F$. It shows that both structures adopt the pyrochlore type $A_2B_2X_6X'$ structure [SG: $Fd\bar{3}m$, Z = 8, a = 10.448(1) Å for the Ta compound and a = 10.448(7) Å for the Nb compound]. The BO_6 octahedra built the classical pyrochlore $[B_2X_6]^{2-}$ array, while the F^- ions are strictly ordered on the 8b positions, which correspond to the centre of the pyrochlore cages. The Li^+, La^{3+} ions and vacancies located in the hexagonal tunnels are assumed to occupy statistically the A sites in the 16d position. The local structure has been more precisely studied by HREM and ^{19}F solid-state NMR techniques. The HREM study reveals significant population fluctuations in the 16d site. ^{19}F MAS NMR spectroscopy evidences six different environments for the fluoride ion, $[FLi_3\square]$ (or $[FLi_4]$), $[FLi_3La]$, $[FLi_2La\square]$, $[FLi_2La_2]$, $[FLiLa_2\square]$ and $[FLa_2\square_2]$, whereas fifteen different types of environment are expected if a random distribution of Li^+, La^{3+} and vacancies in the 16d site is assumed. The solid solution composition domains are limited for the highest Li^+ ions content (low x value) and for the highest La^{3+} ions and vacancies content (high x value) because of the low stability of environments rich in Li^+ or La^{3+} ions. It has been shown that La(Li)–F distances decrease with the CN of F^- ions, from $[FLi_3La]$ to $[FLi_2La\square]$ and from $[FLi_2La_2]$ to $[FLa_2\square_2]$ environments. Fluoride ions occupying tetrahedra involving vacancies are brought closer to the corners occupied by Li^+ and/or La^{3+}. Finally, the stability of the oxyfluoride pyrochlore phases is discussed.

Introduction

Many $A_2B_2O_7$ and $A_2B_2O_6X'$ (X′ = OH, F, S, etc.) phases have been reported[1] to adopt the pyrochlore structure, which originates from the $NaCa(Nb,Ta)O_6(OH/F)$ mineral. This structure can be described as a tri-dimensional network of BO_6 octahedra sharing all their corners, which thus creates large hexagonal tunnels where A cations and X′ anions are located.

In search of new lithium oxyfluorides, we obtained two new examples of oxyfluoride pyrochlore compounds with the formulation $Li_{2-x}La_{(1+x)/3}\square_{(2x-1)/3}B_2O_6F$ (B = Ta, Nb). The structural characterization has been performed by powder and single-crystal X-ray diffraction (XRD) and transmission electron microscopy (TEM). In addition, and as solid-state nuclear magnetic resonance (NMR) spectroscopy is not susceptible to averaging because of distribution and/or disorder, we completed this structural study with high-speed ^{19}F magic angle spinning (MAS) NMR experiments to obtain information on the local environment of the fluoride ions as previously done in $LiCaM_2O_6F$ (M = Ta, Nb) compounds[2] and in the Ce-based fluorite-type oxyfluorides $Ce_{1-x}Ca_xO_{2-x-y/2}F_y$.[3]

The title compounds are two new examples that show the stability of the pyrochlore structure relative to that of the layered perovskite structure. This stability was studied on $A_2B_2O_7$ compounds in 1983[4] and on $A_2B_2O_6F$ compounds recently.[2,5] This point will be discussed at the end of this paper.

Results and Discussion

Structural Study

X-ray Diffraction

Powder Samples

The powder XRD patterns (an example is given in the Supporting Information) of the Ta and Nb materials were

---

[a] Laboratoire des Oxydes et Fluorures (UMR CNRS 6010), Institut de Recherche en Ingénierie Moléculaire et Matériaux Fonctionnels (FR CNRS 2575), Université du Maine,
Avenue O. Messiaen, 72085 Le Mans Cedex 9, France
Fax: +33-2-43833506
E-mail: christophe.legein@univ-lemans.fr
Francoise.Le-Berre@univ-lemans.fr
[b] Laboratoire de Physique de l'Etat Condensé (UMR CNRS 6087), Institut de Recherche en Ingénierie Moléculaire et Matériaux Fonctionnels (FR CNRS 2575), Université du Maine,
Avenue O. Messiaen, 72085 Le Mans Cedex 9, France

Supporting information for this article is available on the WWW under http://dx.doi.org/10.1002/ejic.201000599.

readily indexed in a cubic unit cell presenting an Fd-- extinction symbol with $a \approx 10.5$ Å. A solid solution $Li_{2-x}La_{(1+x)/3}\square_{(2x-1)/3}B_2O_6F$ is evidenced for both, in which x ranges from 0.6 to 1.1 for the Ta compounds and from 0.7 to 1.0 for the Nb compounds. For smaller x values, $LiBO_3$ is present as an impurity, while for higher x values, $Li_{0.5}La_{0.5}B_2O_6$ and LaF_3 are observed. The pattern-matching procedure of the Fullprof program[6] performed in the $Fd\bar{3}m$ space group (n° 227) allows us to follow the evolution of the unit cell parameter with the composition (Figure 1 and Table 1) and to find the limit of the solid solutions. Reliability factors are given in Table 1 for all studied compositions. We observe in Figure 1 that the substitution of three small Li^+ cations (0.92 Å[7]) by only one larger La^{3+} cation (1.16 Å[7]) implies, however, a continuous increase in the cell parameters.

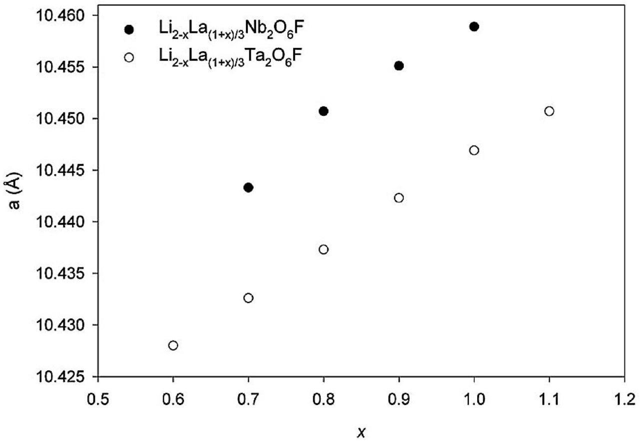

Figure 1. Cell parameter vs. x of the two solid solutions $Li_{2-x}La_{(1+x)/3}\square_{(2x-1)/3}B_2O_6F$.

Table 1. Lattice parameters a [Å] and reliability factors of $Li_{2-x}La_{(1+x)/3}\square_{(2x-1)/3}B_2O_6F$ (B = Nb, Ta).

x	Ta	$R_p/R_{wp}/\chi^2$	Nb	$R_p/R_{wp}/\chi^2$
0.6	10.4280(1)	7.63/8.04/4.46		
0.7	10.4326(1)	8.19/9.27/6.73	10.4433(1)	8.31/8.28/4.12
0.8	10.4373(1)	6.89/7.01/4.72	10.4507(1)	7.77/7.81/4.38
0.9	10.4423(1)	7.20/8.25/6.95	10.4551(1)	8.91/8.63/4.60
1.0	10.4469(1)	7.21/8.68/9.03	10.4589(1)	8.68/8.30/3.68
1.1	10.4507(1)	7.91/7.83/3.33		

Single Crystals

The operating conditions for the data collection on a small single crystal for both compounds are given in the experimental section. The lattice parameters (10.448 Å for both) were refined by the double scan technique from the positions of 30 reflections in the vicinity of 30° (2θ). The structure refinements were carried out in the $Fd\bar{3}m$ space group. The direct methods reveal two positions for the heavy atoms: 16d and 16c sites. According to the classical description of the pyrochlore structural type, La^{3+} ions are placed on the 16d site (1/2, 1/2, 1/2), while B^{5+} ions occupy the 16c site (0, 0, 0). Subsequent Fourier-difference synthesis allows to complete the structure with two anionic positions corresponding to the 48f and 8b sites: O^{2-} ions in the 48f site (x, 1/8, 1/8) – with $x \approx 0.32$ – and F^- ions in the 8b site (3/8, 3/8, 3/8). At this stage, no information with regard to the location of the Li^+ ions can be obtained on the Fourier-difference map. We then proposed to locate the Li^+ ions, with the La^{3+} ions on the 16d site, for both compounds. The lanthanum occupancy in the 16d site is refined, while the lithium quantity is adjusted to obtain electrical neutrality; the last refinement leads to a partial occupancy of the 16d site and to the following formulations: $Li_{1.00}La_{0.67}\square_{0.33}Ta_2O_6F$ and $Li_{1.25}La_{0.58}\square_{0.17}Nb_2O_6F$. We note that the cell parameters refined from single crystals are in good agreement with those deduced by powder XRD (Table 1 and Figure 1). With anisotropic thermal parameters for all species, weighting scheme, secondary extinction, and 11 adjustable parameters, the refinement of the final stage converges to satisfactory R indexes values (see Experimental Section). For the Ta compound, the final Fourier-difference synthesis map presents subsequent maxima and minima peaks, at around $\pm 4e^-/Å^3$, located near the Ta^{5+} positions. Fractional atomic coordinates and isotropic thermal B_{eq} parameters are gathered in Table 2, while Table 3 presents characteristic selected interatomic distances and angles. Figure 2 shows a view of the structure, which can be described by a three-dimensional network of BO_6 octahedra sharing corners. The resulting framework creates large hexagonal tunnels in which La^{3+}/Li^+ ions and vacancies are located, while the F^- ions occupy the centre of the pyrochlore cages. The BO_6 octahedra are regular with six equal B–O distances of 1.973 Å, close to the sum of the ionic radii {1.99 Å [0.64 Å for $(R_{B^{5+}})^{VI}$ + 1.35 Å for $(R_{O^{2-}})^{II}$]}[7] and similar to the Ta–O distance in the isostructural compound

Table 2. Atomic coordinates and isotropic thermal parameter B_{eq} for $Li_{1.00}La_{0.67}\square_{0.33}Ta_2O_6F$ and $Li_{1.25}La_{0.58}\square_{0.17}Nb_2O_6F$ (in italic).

Atom	Site	x	y	z	sof	B_{eq} [Å]
Ta	16c	0	0	0	1	0.85(2)
Nb	*16c*	*0*	*0*	*0*	*1*	*1.15(2)*
La/Li/□	16d	1/2	1/2	1/2	0.33/0.5/0.17	1.68(6)
La/Li/□	*16d*	*1/2*	*1/2*	*1/2*	*0.29/0.62/0.09*	*1.46(2)*
O	48f	0.3164(7)	1/8	1/8	1	1.26(9)
O	*48f*	*0.3165(2)*	*1/8*	*1/8*	*1*	*1.18(4)*
F	8b	3/8	3/8	3/8	1	6.3(9)
F	*8b*	*3/8*	*3/8*	*3/8*	*1*	*5.9(3)*

$Ca_{1.5}Ta_2O_6F$[2] (1.982 Å). The $F^–$ ions, which do not take part in the $(B_2O_6)^{2–}$ network can therefore be considered as "independent". They are tetrahedrally coordinated by La^{3+}/Li^+ ions and vacancies at an average distance of 2.262 Å. For comparison, the Li–F and La–F distances calculated from ionic radii[7] are 2.23 Å and 2.49 Å, respectively. The La^{3+}/Li^+ ions are in a 2+6 coordination mode (two $F^–$ at 2.262 Å and six $O^{2–}$ at 2.663 Å). In Table 4, we compare the calculated valence sum[8] for all the ions to the theoretical values. We observe that the vacancies on the 16d site always lead to smaller values than those expected, with the exception of the B^{5+} ions, which are only surrounded by $O^{2–}$ anions. It shows that the XRD technique gives average $La^{3+}/Li^+/\square–O^{2–}$ or $La^{3+}/Li^+/\square–F^–$ distances and does not reflect the exact local situation.

Table 3. Selected interatomic distances [Å] and angles [°] for $Li_{1.00}La_{0.67}\square_{0.33}Ta_2O_6F$ and $Li_{1.25}La_{0.58}\square_{0.17}Nb_2O_6F$.

	$Li_{1.00}La_{0.67}\square_{0.33}Ta_2O_6F$	$Li_{1.25}La_{0.58}\square_{0.17}Nb_2O_6F$
Ta/Nb octahedron	Ta–O: 6 × 1.973(2)	Nb–O: 6 × 1.9732(9)
	O–Ta–O: 180	O–Nb–O: 180
	O–Ta–O: 88.4(3)	O–Nb–O: 88.4(1)
	O–Ta–O: 91.6(3)	O–Nb–O: 91.6(1)
F environment	F–La/Li/□: 4 × 2.2620(2)	F–La/Li/□: 4 × 2.2621(2)
	La/Li/□-F–La/Li/□: 109.47	La/Li/□-F–La/Li/□: 109.47
La/Li/□ environment	La/Li/□-O: 6 × 2.663(5)	La/Li/□-O: 6 × 2.662(2)
	La/Li/□-F: 2 × 2.2620(2)	La/Li/□-F: 2 × 2.2621(2)
	O–La/Li/□-O: 180	O–La/Li/□-O: 180
	O–La/Li/□-O: 62.22(5)	O–La/Li/□-O: 62.23(2)
	O–La/Li/□-O: 117.78(5)	O–La/Li/□-O: 117.77(2)
	O–La/Li/□-F: 81.4(1)	O–La/Li/□-F: 81.34(4)
	O–La/Li/□-O: 98.6(1)	O–La/Li/□-O: 98.66(4)
	F–La/Li/□-F: 180	F–La/Li/□-F: 180

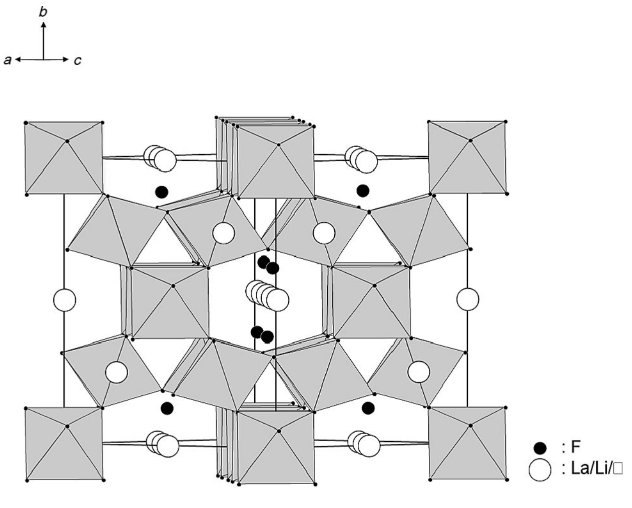

Figure 2. Structure of the pyrochlores $Li_{2–x}La_{(1+x)/3}\square_{(2x–1)/3}B_2O_6F$ showing the hexagonal tunnels.

Table 4. Valence bond analysis for $Li_{1.00}La_{0.67}\square_{0.33}Ta_2O_6F$ and $Li_{1.25}La_{0.58}\square_{0.17}Nb_2O_6F$.

$Li_{1.00}La_{0.67}\square_{0.33}Ta_2O_6F$		
Ta	$v_{Ta–O} = 0.866$	$\Sigma v = 0.866 \times 6 = 5.2/5$[a]
La/Li	$v_{La/Li–O} = 0.084$	
	$v_{La/Li\,–\,F} = 0.186$	$\Sigma v = 0.084 \times 6 + 0.186 \times 2 = 0.9/1.8$[a]
O	$v_{O–Ta} = 0.866$	
	$v_{O–La/Li} = 0.084$	$\Sigma v = 0.866 \times 2 + 0.084 \times 2 = 1.9/2$[a]
F	$v_{F–La/Li} = 0.186$	$\Sigma v = 0.186 \times 4 = 0.7/1$[a]
$Li_{1.25}La_{0.58}\square_{0.17}Nb_2O_6F$		
Nb	$v_{Nb–O} = 0.846$	$\Sigma v = 0.846 \times 6 = 5.1/5$[a]
La/Li	$v_{La/Li–O} = 0.068$	
	$v_{La/Li–F} = 0.151$	$\Sigma v = 0.068 \times 6 + 0.151 \times 2 = 0.7/1.8$[a]
O	$v_{O–Ta} = 0.846$	
	$v_{O–La/Li} = 0.068$	$\Sigma v = 0.846 \times 2 + 0.068 \times 2 = 1.8/2$[a]
F	$v_{F–La/Li} = 0.151$	$\Sigma v = 0.151 \times 4 = 0.6/1$[a]

[a] Expected value.

Transmission Electron Microscopy

These experiments were performed on the Ta compound. An EDX analysis of more than 20 microcrystals with a KEVEX energy dispersive X-ray spectrometer coupled with the TEM revealed always the simultaneous presence of Ta, La, O and F. A selected area electron diffraction (SAED) study, carried out on a number of crystals that were rotated to scan the reciprocal space, reveals a very good crystallinity of the sample and a cubic unit cell with $a \approx 10.4$ Å. Electron diffraction patterns of three different zone axis orientations [100], [110] and [111] are shown in Figure 3. The systematic absences allow the deduction of the extinction symbol Fd-- compatible only with the two space groups $Fd\bar{3}m$ (centric, N° 227) and $Fd\bar{3}$ (acentric, N° 203), according to the results of the XRD study. The existence of the forbidden reflection *00l*, $l = 2n$ on a [110] zone axis pattern (Figure 3b) is due without doubt to a double diffraction phenomenon, as it is possible to make them disappear while tilting along [00l]* reciprocal rows, which confirms the *00l* ($l = 4n$) condition. Moreover, such reflections are missing in Figure 3a.

For the high-resolution electron microscope (HREM) study, we chose to observe the crystallites with the electron beam parallel to the [110] direction, which gives the best description of atom stacking. A typical observed image is shown in Figure 4 in which the SAED pattern and the simulated image are inserted for a crystal thickness of about 30 Å and a defocus value of 14 nm. Under these conditions, La/Li/□ columns can be correlated to the brightest dots, while the least-bright dots are associated with Ta or La/Li/□/Ta atom columns. A good agreement is obtained between the observed image and that calculated from the atomic positions refined from single-crystal XRD data. However, a careful examination of the HREM observed image reveals that some bright dots corresponding to La/Li/□ columns are more or less intense (see white arrows on Figure 4), which implies locally a 16d site occupation different from the nominal value. Indeed, a statistical distribution of La/Li/□ on the 16d site would imply a regular contrast. Consequently, the occupation of the 16d site obtained from the XRD study is averaged and does not reflect the exact local population.

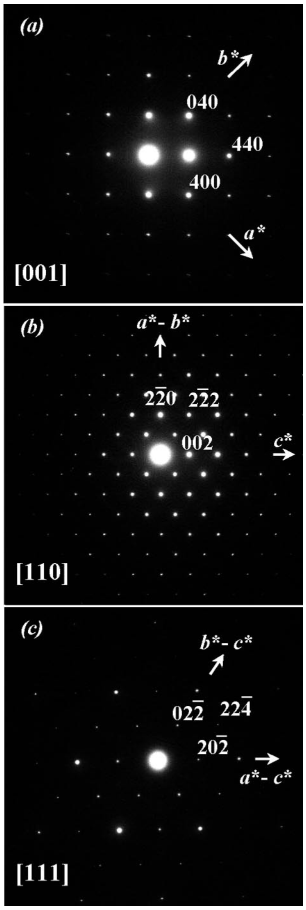

Figure 3. Typical SAED patterns of $Li_{1.00}La_{0.67}\square_{0.33}Ta_2O_6F$ crystallites with three different zone axis orientations (a) [100], (b) [110] and (c) [111].

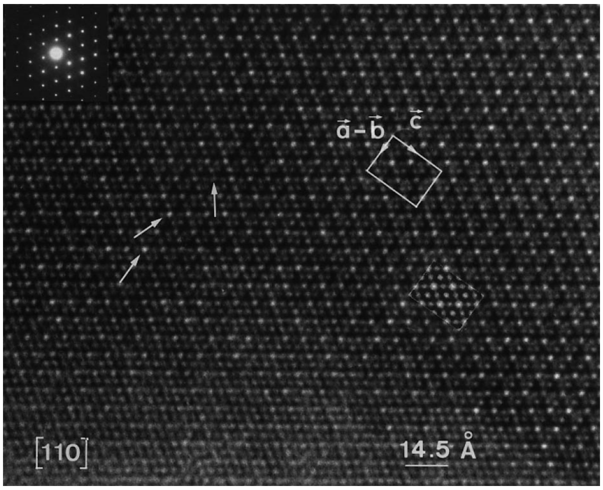

Figure 4. [110] HREM image of a $Li_{1.00}La_{0.67}\square_{0.33}Ta_2O_6F$ crystallite with the SAED pattern and the simulated image inserted. White arrows show more or less pronounced bright dots corresponding to the La/Li/□ columns.

Local Environments of the Fluoride Ions Probed by ^{19}F MAS NMR Spectroscopy

As XRD is not able to differentiate between the different environments of the fluoride ions, high-speed ^{19}F MAS NMR spectroscopy has been used. This study involves four powder samples of each solid solution $Li_{2-x}La_{(1+x)/3}\square_{(2x-1)/3}B_2O_6F$ (B = Ta, Nb) with $x = 0.7$, 0.8, 0.9 and 1.0. In these oxyfluorides, two anion sites are possible, a priori: 48f and 8b. The environments of these crystallographic sites are: 2 B (Ta or Nb) at ca. 1.97 Å and 2 La/Li/□ at ca. 2.66 Å for the first and 4 La/Li/□ at ca. 2.26 Å for the second (Table 3).

The ^{19}F NMR spectra as a function of x are presented in Figures 5 and 6 for the Ta and Nb compounds, respectively. The experimental and calculated ^{19}F NMR spectra of $Li_{2-x}La_{(1+x)/3}\square_{(2x-1)/3}Ta_2O_6F$ are presented in Figure 7 for $x = 0.8$ and $x = 1.0$, as examples. The other calculated ^{19}F NMR spectra are given in the Supporting Information. The parameters used for the reconstruction of the experimental spectra are gathered in Tables 5 and 6. For both solid solutions, the ^{19}F NMR spectra show four isotropic lines for $x = 0.7$ and 0.8 and five for $x = 0.9$ and 1.0. There are six distinct possible environments for the 48f sites: $[B_2La_2]$, $[B_2LaLi]$, $[B_2Li_2]$, $[B_2La\square]$, $[B_2Li\square]$ and $[B_2\square_2]$. For $x = 0.7$ for example, the calculated probabilities for the occurrence of each of these environments, assuming a random distribution of Li^+, La^{3+} and □ in the 16d site, are 8.0%, 36.8%, 42.3%, 3.8%, 8.7% and 0.4%, respectively. Whatever the assignment of the four ^{19}F NMR lines (Figure 5, Table 5), no agreement can be obtained between the composition and the ^{19}F NMR line relative intensities by assuming that fluoride ions are located on the 48f site. Moreover, whereas the δ_{iso} values of most of these lines increase with x (see Figures 5 and 6 and Tables 5 and 6), for the same value of x, the δ_{iso} values are approximately equal for $Li_{2-x}La_{(1+x)/3}\square_{(2x-1)/3}Ta_2O_6F$ and $Li_{2-x}La_{(1+x)/3}\square_{(2x-1)/3}Nb_2O_6F$ (Tables 5 and 6); the highest difference is around 3 ppm. We can conclude that, in both compounds, the environments of the fluoride ions are similar, i.e. are not dependent on the nature of the metal B that occupies the 16c sites. This shows that fluoride ions are located exclusively on the 8b site, at the centre, on average, of the $[FLi_nLa_m\square_{4-n-m}]$ tetrahedra, in agreement with XRD study and valence bond analysis for the O atoms (Table 4). This confirms the great affinity of the most electronegative atom, F (Pauling scale electronegativities: χ_F 3.98, χ_O 3.44), for electropositive atoms, as previously observed in oxyfluoride pyrochlores $LiCaB_2O_6F$ and $Ca_{1.5}\square_{0.5}B_2O_6F$ (B = Nb and Ta)[2] and in Ce-based fluorite-type oxyfluorides.[3] Lithium and lanthanum (χ_{Li} 0.98, χ_{La} 1.10) are indeed more electropositive than tantalum and niobium (χ_{Ta} 1.5, χ_{Nb} 1.6).

The line widths do not depend on the spinning frequency between 30 and 34 kHz, which indicates that heteronuclear and homonuclear dipolar interactions are fully averaged at 30 kHz. The line widths of the NMR resonances then mirror the isotropic chemical shift distributions. This may be related to the occupancy of the 16d crystallographic site by Li^+ and La^{3+} cations as well as by vacancies that lead to

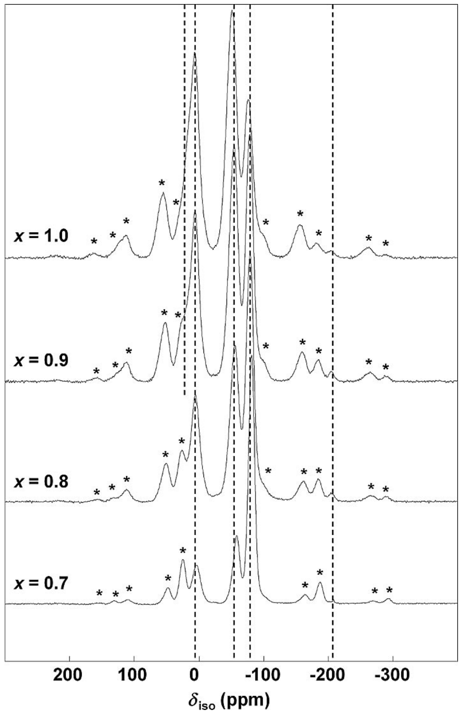

Figure 5. ^{19}F MAS (30 kHz) NMR spectra of $Li_{2-x}La_{(1+x)/3}\square_{(2x-1)/3}Ta_2O_6F$ with x = 0.7, 0.8, 0.9 and 1.0. The stars indicate the main spinning sidebands. The dashed lines indicate the isotropic ^{19}F NMR lines. The line with the highest δ_{iso} value exists only for x = 0.9 and x = 1.0.

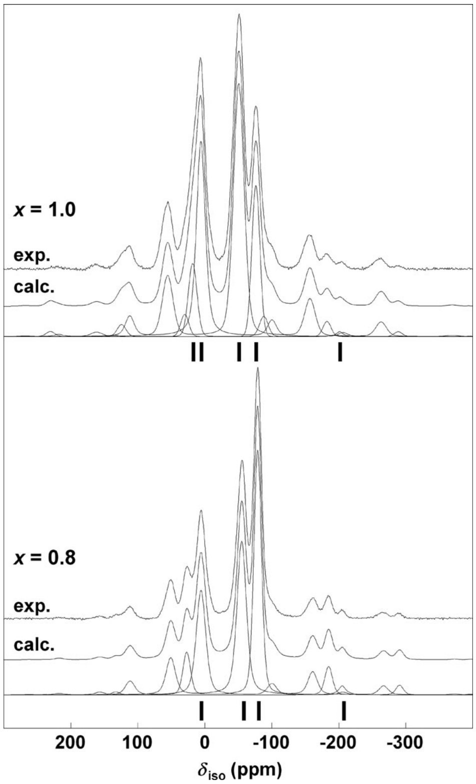

Figure 7. Experimental (exp.) and calculated (calcd.) ^{19}F MAS (30 kHz) NMR spectra of $Li_{2-x}La_{(1+x)/3}\square_{(2x-1)/3}Ta_2O_6F$ with x = 0.8 and 1.0. The individual contributions to the reconstructed spectra are shown below. The sticks indicate the isotropic ^{19}F NMR lines.

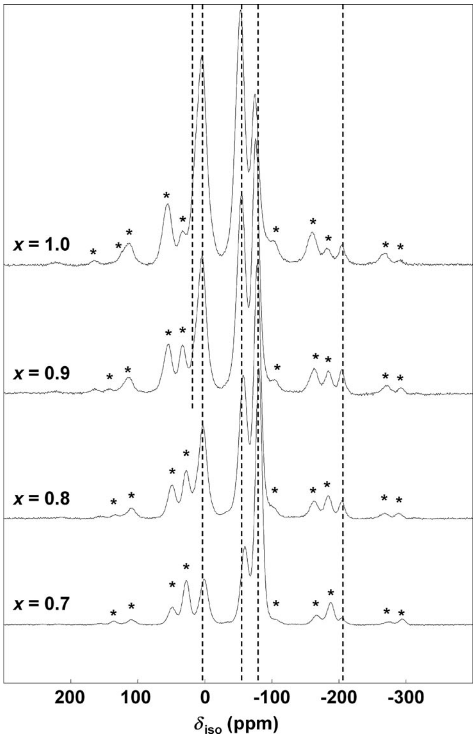

Figure 6. ^{19}F MAS (30 kHz) NMR spectra of $Li_{2-x}La_{(1+x)/3}\square_{(2x-1)/3}Nb_2O_6F$ with x = 0.7, 0.8, 0.9 and 1.0. The stars indicate the main spinning sidebands. The dashed lines indicate the isotropic ^{19}F NMR lines. The line with the highest δ_{iso} value exists only for x = 0.9 and x = 1.0.

various F–Li and F–La bond lengths. Whereas there are fifteen distinct possible environments [$FLi_nLa_m\square_{4-n-m}$] for the fluoride ions, the ^{19}F NMR spectra show evidence of only four or five (depending on the x value) isotropic lines. The calculated probabilities for the occurrence of these possible environments, by assuming, as above, a random distribution of Li^+, La^{3+} and $\square$ in the 16d site, are gathered in Table 7. Nevertheless, some environments can readily be ruled out from a steric, electrostatic or statistical standpoint. The 16d site is eightfold coordinated. For this coordination number (CN), $r(^{VIII}Li^+)$ = 0.92 Å and $r(^{VIII}La^{3+})$ = 1.16 Å.[7] The average CN of the F^- ion ranges from 3.74 for x = 0.7 to 3.33 for x = 1, and the ionic radius of the F^- ions ranges from 1.285 Å for CN = 2 to 1.31 Å for CN = 4.[7] Depending on the CN of the F^- ions, the sums of the ionic radii range from 2.205 Å to 2.23 Å for the F^- and Li^+ ions and from 2.245 Å to 2.47 Å for the F^- and La^{3+} ions. Owing to the very short average distance between the 8b and 16d sites, which ranges from 2.261 (2.259) Å for x = 0.7 to 2.264 (2.263) Å for x = 1 for $Li_{2-x}La_{(1+x)/3}\square_{(2x-1)/3}Ta_2O_6F$ ($Li_{2-x}La_{(1+x)/3}\square_{(2x-1)/3}Nb_2O_6F$) compounds, the environments [FLa_4], [$FLiLa_3$] and [$FLa_3\square$] can be ruled out. Fluoride ions are threefold coordinated in LaF_3,[9] but the distances between the La^{3+} and F^- ions range from 2.4 Å to 2.5 Å, in good agreement with the sum of the ionic radius, which is equal to 2.516 Å [$r(^{IX}La^{3+})$ = 1.216 Å and

Table 5. Isotropic chemical shifts (ppm), line widths (ppm) and relative intensities (%) of the ^{19}F NMR lines for $Li_{2-x}La_{(1+x)/3}\square_{(2x-1)/3}Ta_2O_6F$ with x = 0.7, 0.8, 0.9 and 1.0, the number of Li^+, La^{3+} and vacancy in the corresponding fluoride ion environments $[FLi_nLa_m\square_{4-n-m}]$, the number of Li^+, La^{3+} and vacancy multiplied by the relative intensity (i.e. the proportion of fluoride ion adopting this environment) and the number of Li^+, La^{3+} and vacancy per formula (in bold). In italic, the occurrence of $[FLiLa_2\square]$ is assumed.

x = 0.7 - $Li_{1.30}La_{0.57}\square_{0.13}Ta_2O_6F$									
Line	δ_{iso}	LW	I	Li	La	□	Li	La	□
1	–208.1	2.0	0.1	3	0	1	0.003	0	0.001
2	–81.4	11.1	65.5	3	1	0	1.965	0.655	0
3	–58.1	12.7	22.7	2	1	1	0.454	0.227	0.227
4	3.8	15.1	11.6	2	2	0	0.232	0.232	0
							1.33	**0.56**	**0.11**
x = 0.8 - $Li_{1.20}La_{0.60}\square_{0.20}Ta_2O_6F$									
Line	δ_{iso}	LW	I	Li	La	□	Li	La	□
1	–205.3	13.3	1.4	3	0	1	0.042	0	0.014
2	–79.0	13.3	40.3	3	1	0	1.209	0.403	0
3	–55.1	16.4	36.8	2	1	1	0.736	0.368	0.368
4	5.6	16.7	21.5	2	2	0	0.43	0.43	0
							1.21	**0.60**	**0.19**
x = 0.9 - $Li_{1.10}La_{0.63}\square_{0.27}Ta_2O_6F$									
Line	δ_{iso}	LW	I	Li	La	□	Li	La	□
1	–204.9	12.4	1.4	3	0	1	0.042	0	0.014
2	–78.3	13.0	28.8	3	1	0	0.864	0.288	0
3	–53.7	16.8	41.5	2	1	1	0.83	0.415	0.415
4	5.6	14.9	21.8	2	2	0	0.436	0.436	0
4	*5.6*	*14.9*	*21.8 – y*	*2*	*2*	*0*	*0.436–2y*	*0.436–2y*	*0*
			2y	*1*	*2*	*1*	*2y*	*4y*	*2y*
5	18.4	15.0	6.5	0	2	2	0	0.13	0.13
5	*18.4*	*15.0*	*6.5 – y*	*0*	*2*	*2*	*0*	*0.13–2y*	*0.13–2y*
							1.09	**0.63**	**0.28**
x = 1.0 - $Li_{1.00}La_{0.67}\square_{0.33}Ta_2O_6F$									
Line	δ_{iso}	LW	I	Li	La	□	Li	La	□
1	–201.3	11.3	0.5	3	0	1	0.015	0	0.005
2	–76.3	14.1	16.4	3	1	0	0.492	0.164	0
3	–50.8	18.8	46.2	2	1	1	0.924	0.462	0.462
4	5.7	15.7	27.0	2	2	0	0.54	0.54	0
4	*5.7*	*15.7*	*27.0 – z*	*2*	*2*	*0*	*0.54–2z*	*0.54–2z*	*0*
			2z	*1*	*2*	*1*	*2z*	*4 z*	*2z*
5	18.1	15.2	9.9	0	2	2	0	0.198	0.198
5	*18.1*	*15.2*	*9.9 – z*	*0*	*2*	*2*	*0*	*0.198–2z*	*0.198–2z*
							0.99	**0.68**	**0.33**

$r(^{III}F^-)$ = 1.30 Å[7]]. Moreover, the calculated probabilities for the occurrence of $[FLa_4]$ and $[FLa_3\square]$ are small. On the other hand, in the $[F\square_4]$, $[FLi\square_3]$ and $[FLa\square_3]$ environments, the small number of counterions induces electrostatic repulsion between the F^- and O^{2-} ions, and these environments are then not stable. Moreover, they present low calculated probabilities of occurrence. At last, owing to the long average distances between the 8b and 16d sites, the environments that involve two vacancies and at least one Li^+ ion, i.e. $[FLi_2\square_2]$ and $[FLiLa\square_2]$, are probably unstable and could also be ruled out. Of the seven remaining environments ($[FLi_4]$, $[FLi_3\square]$, $[FLi_3La]$, $[FLi_2La\square]$, $[FLi_2La_2]$, $[FLiLa_2\square]$ and $[FLa_2\square_2]$), which ones really exist, and is it possible to relate the ^{19}F NMR lines to these environments?

We will answer these questions in the following section with the help of the ^{19}F NMR study of the $Li_{2-x}La_{(1+x)/3}\square_{(2x-1)/3}Ta_2O_6F$ compounds. As the main results are similar for the $Li_{2-x}La_{(1+x)/3}\square_{(2x-1)/3}Nb_2O_6F$ series, the ^{19}F NMR study of these compounds will be briefly discussed hereafter to avoid a long and repetitive discussion. From this point, the ^{19}F NMR resonances are referred as lines 1–5 (Tables 5 and 6), and the corresponding isotropic chemical shifts are noted as $\delta_{iso}(i)$ with i = 1–5. The relative intensity of these lines depends on x (Figure 8). The ^{19}F δ_{iso} values are roughly between the values in LiF (–204 ppm[10]) and in LaF_3 (in the range –23 to 18 ppm[11,12]). Nevertheless, as previously mentioned, F^- ions are threefold coordinated in LaF_3,[9] and the distances between the La^{3+} and F^- ions range from 2.4 Å to 2.5 Å. In LiF,[13] F^- ions are sixfold coordinated, and the distance between the Li^+ and F^- ions is equal to 2.013 Å. The CN of the F^- ions are then different in both basic fluorides and in the studied compounds, where, additionally, the CN of the F^- ions is different from one environment to another. Accordingly, the approach often used, based on the intuitive idea that similar structural environments produce similar δ_{iso} values, cannot be efficient and the assignments of the resonances to different distributions of Li^+ and La^{3+} cations and vacancies around the fluoride ions cannot be straightforward. In order to achieve these assignments, we have to take into account,

Table 6. Isotropic chemical shifts (ppm), line widths (ppm) and relative intensities (%) of the ^{19}F NMR lines for $Li_{2-x}La_{(1+x)/3}\square_{(2x-1)/3}Nb_2O_6F$ with $x = 0.7$, 0.8, 0.9 and 1.0, the number of Li^+, La^{3+} and vacancy in the corresponding fluoride ion environments $[FLi_nLa_m\square_{4-n-m}]$, the number of Li^+, La^{3+} and vacancy multiplied by the relative intensity (i.e. the proportion of fluoride ion adopting this environment) and the number of Li^+, La^{3+} and vacancy per formula (in bold).

$x = 0.7$ - $Li_{1.30}La_{0.57}\square_{0.13}Nb_2O_6F$

Line	δ_{iso}	LW	I	Li	La	□	Li	La	□
1	–205.4	6.6	0.7	3	0	1	0.021	0	0.007
2	–80.7	11.9	61.6	3	1	0	1.848	0.616	0
3	–59.7	14.1	24.2	2	1	1	0.484	0.242	0.242
4	1.2	15.0	13.5	2	2	0	0.270	0.270	0
							1.31	**0.56**	**0.12**

$x = 0.8$ - $Li_{1.20}La_{0.60}\square_{0.20}Nb_2O_6F$

Line	δ_{iso}	LW	I	Li	La	□	Li	La	□
1	–204.8	8.3	2.1	3	0	1	0.063	0	0.021
2	–78.7	12.2	47.5	3	1	0	1.425	0.475	0
3	–57.3	14.2	32.3	2	1	1	0.646	0.323	0.323
4	3.2	16.3	18.1	2	2	0	0.362	0.362	0
							1.25	**0.58**	**0.17**

$x = 0.9$ - $Li_{1.10}La_{0.63}\square_{0.27}Nb_2O_6F$

Line	δ_{iso}	LW	I	Li	La	□	Li	La	□
1	–204.5	8.5	1.7	3	0	1	0.051	0	0.017
2	–76.3	12.1	35.2	3	1	0	1.056	0.352	0
3	–54.4	15.1	37.3	2	1	1	0.746	0.373	0.373
4	4.2	15.7	21.6	2	2	0	0.432	0.432	0
5	18.6	15.3	4.2	0	2	2	0	0.084	0.084
							1.14	**0.62**	**0.24**

$x = 1.0$ - $Li_{1.00}La_{0.67}\square_{0.33}Nb_2O_6F$

Line	δ_{iso}	LW	I	Li	La	□	Li	La	□
1	–204.4	9.5	1.5	3	0	1	0.045	0	0.015
2	–75.3	13.5	20.6	3	1	0	0.618	0.206	0
3	–52.8	16.1	41.5	2	1	1	0.830	0.415	0.415
4	4.1	17.0	29.9	2	2	0	0.598	0.598	0
5	15.9	13.2	6.5	0	2	2	0	0.130	0.130
							1.05	**0.67**	**0.28**

Table 7. Calculated probabilities (%) for the occurrence of the fluoride ion environments $[FLi_nLa_m\square_{4-n-m}]$, by assuming a statistical distribution, in the $Li_{2-x}La_{(1+x)/3}\square_{(2x-1)/3}B_2O_6F$ (B = Ta, Nb) compounds with $x = 0.7$, 0.8, 0.9 and 1.0.

$Li_{1.30}La_{0.57}\square_{0.13}B_2O_6F$				**n**		
		0	**1**	**2**	**3**	**4**
m	**0**	0.00	0.08	1.13	7.32	17.85
	1	0.03	0.98	9.58	31.12	
	2	0.21	4.17	20.35		
	3	0.61	5.91			
	4	0.64				

$Li_{1.20}La_{0.60}\square_{0.20}B_2O_6F$				**n**		
		0	**1**	**2**	**3**	**4**
m	**0**	0.01	0.24	2.16	8.64	12.96
	1	0.12	2.16	12.96	25.92	
	2	0.54	6.48	19.44		
	3	1.08	6.48			
	4	0.81				

$Li_{1.10}La_{0.63}\square_{0.27}B_2O_6F$				**n**		
		0	**1**	**2**	**3**	**4**
m	**0**	0.03	0.52	3.23	8.87	9.15
	1	0.30	3.72	15.33	21.07	
	2	1.07	8.82	18.20		
	3	1.69	6.99			
	4	1.01				

$Li_{1.00}La_{0.67}\square_{0.33}B_2O_6F$				**n**		
		0	**1**	**2**	**3**	**4**
m	**0**	0.08	0.93	4.17	8.33	6.25
	1	0.62	5.56	16.67	16.67	
	2	1.85	11.11	16.67		
	3	2.47	7.41			
	4	1.23				

qualitatively, the cation–fluorine distances. This can be achieved by the use of the superposition model,[14] which allows the assignment of isotropic chemical shifts to fluorine crystallographic sites through the use of phenomenological parameters. In this model, the ^{19}F isotropic chemical shift is considered as a sum of one constant diamagnetic term and several paramagnetic contributions from the l neighbouring cations (M) and is calculated according to the main following formula: $\delta_{iso/C_6F_6} = -127.1 - \sum_l \sigma_l$ ppm and $\sigma_l = \sigma_{l_0}\exp[-a_l(d-d_0)]$. d_0 is the characteristic F–M distance, which is equal to the bond length in the related basic fluoride and, σ_{l_0} is the parameter that determines the order of magnitude of the cationic paramagnetic contribution to the shielding and is deduced from measurements in the related basic fluoride, where $\delta_{iso/C_6F_6} = -127.1 - n\sigma_{l_0}$ (n is the CN of the fluorine atom). This model was successfully applied to fluorides[14–18] and oxyfluorides.[2,3] For the qualitative approach presented below, it may be underlined that: (i) σ_{l_0}, the cationic paramagnetic contribution to the shielding of La^{3+} is higher than that for Li^+, (ii) the ^{19}F δ_{iso} value increases with CN (F–M distances remaining equal) and (iii) the ^{19}F δ_{iso} value increases if F–M distances decrease (for the same CN).

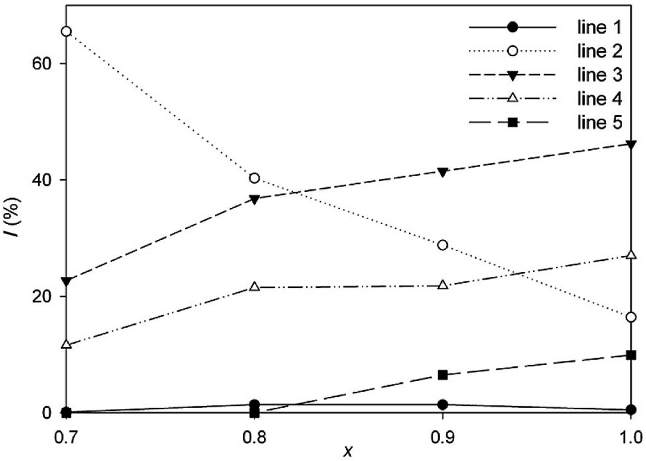

Figure 8. ^{19}F NMR line relative intensities vs. x in the $Li_{2-x}La_{(1+x)/3}\square_{(2x-1)/3}Ta_2O_6F$ series.

The $\delta_{iso}(1)$ values are close (Table 5) to the ^{19}F δ_{iso} value in LiF (–204 ppm).[10] If the occurrence of the LiF impurity can be excluded since these values change with x, these values indicate environments for the F^- ions exclusively built up from Li^+ ions. Among the seven remaining environments, two fulfill this requirement: $[FLi_3\square]$ and $[FLi_4]$. These lines are tentatively assigned to the environment $[FLi_3\square]$ because the agreement between the numbers of Li^+, La^{3+} and vacancy per formula deduced from the relative intensities of the ^{19}F NMR lines and the nominal chemical composition (Table 5) is better than with the environment $[FLi_4]$. Nevertheless, these lines present low relative intensities whatever the x value (Figure 8). Their assignment to the environment $[FLi_4]$ modifies, but slightly, the results of the calculation presented in Table 5 and then cannot be fully ruled out. These low relative intensities are surprising, at first sight, compared to the calculated probabilities for the occurrence of $[FLi_3\square]$ and $[FLi_4]$ (Table 7). Actually, it proves the low stability of these environments, which generate short Li–F distances [shorter than in LiF according to the superposition model and to the $\delta_{iso}(1)$ values] and consequently constrains the adjacent $[FLi_nLa_m\square_{4-n-m}]$ tetrahedra.

The $\delta_{iso}(2,3)$ values are higher than the $\delta_{iso}(1)$ values, which show that the corresponding environments involve at least one La^{3+} cation. The relative intensity of line 2 decreases with increasing x value, i.e. with decreasing Li content and increasing La and □ contents. On the other hand, the relative intensity of line 3 increases with x values (Table 5 and Figure 8). Then, relative to the nominal composition, the environment corresponding to line 2 involves more Li^+ cations, while that corresponding to line 3 involves more (La,□) species. These lines can then be assigned to the environments $[FLi_3La]$ and $[FLi_2La\square]$, respectively. As $\delta_{iso}(3)$ values are higher than $\delta_{iso}(2)$ values, these assignments are surprising, at first sight, since δ_{iso} increases with CN. Nevertheless, these assignments cannot be inverted considering the relative intensity of lines 2 and 3 and the vacancy content (Table 5). The higher value of $\delta_{iso}(3)$ can be explained by noticeably shorter F–La and F–Li distances in $[FLi_2La\square]$, in agreement with a lower CN for this environment. As $[FLi_nLa_m\square_{4-n-m}]$ tetrahedra are connected to each other by corners, Li^+ and La^{3+} cations belong to two tetrahedra. If a cation moves closer to the F^- ion of a tetrahedron, it moves away from the F^- ion of the other tetrahedron. The shorter F–La and F–Li distances (Figure 9) mainly arise as a result of the shift of the fluoride ions toward the occupied corners of the $[FLi_nLa_m\square_{4-n-m}]$ tetrahedra. This phenomenon was already observed in the isostructural β-$Ca_{1.5}\square_{0.5}B_2O_6F$ (B = Nb, Ta) phases, where it has been shown that the fluoride ions are only, on average, at the centre of the $[FCa_3\square]$ tetrahedron and are brought closer to the Ca^{2+} corners.[2]

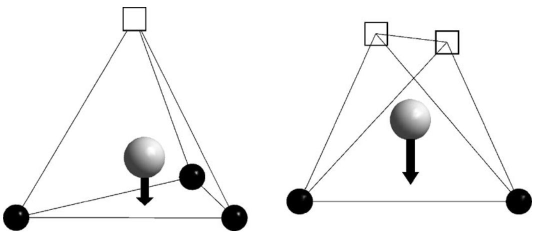

Figure 9. Fluoride ion environments showing the assumed displacements of the fluoride ions resulting from the occurrence of one (left) or two (right) vacancies (□). The grey spheres represent the fluoride ions and the black spheres represent the La^{3+} and/or the Li^+ ions.

The $\delta_{iso}(4,5)$ values are higher than the $\delta_{iso}(2,3)$, which shows that the corresponding environments involve two La^{3+} cations. The relative intensity of these lines increases with x values, i.e. with decreasing Li content and increasing La and □ contents (Table 5 and Figure 8). As for line 3, the corresponding environments involve more (La,□) than on average. The three remaining environments, $[FLi_2La_2]$, $[FLiLa_2\square]$ and $[FLa_2\square_2]$, fulfill this condition and $[FLi_2La_2]$ and $[FLa_2\square_2]$ are assigned to lines 4 and 5, respectively, because these assignments allow the obtaining of a better agreement between the numbers of Li^+, La^{3+} and vacancy per formula deduced from the relative intensities of the ^{19}F NMR lines and the nominal chemical composition (Table 5). Even if the ^{19}F NMR spectra were correctly reconstructed with four or five lines and then do not show evidence of $[FLiLa_2\square]$ environments, the absence of these environments is difficult to justify whereas $[FLa_2\square_2]$ environments occur (for $x = 0.9$ and $x = 1.0$), and the calculated probabilities for the $[FLiLa_2\square]$ environment are higher than for the $[FLa_2\square_2]$ environment (Table 7). By considering the overlapping of lines 4 and 5, the line corresponding to the $[FLiLa_2\square]$ environment, whose δ_{iso} value should be between $\delta_{iso}(4)$ and $\delta_{iso}(5)$, is certainly hidden. According to this assumption, the relative intensities of lines 4 and 5 should be reduced to similar quantities for the maintenance of the numbers of Li^+, La^{3+} and vacancy per formula deduced from the relative intensities of the ^{19}F NMR lines (Table 5). As observed for $[FLi_3La]$ and $[FLi_2La\square]$, an increase in the δ_{iso} values is observed from $[FLi_2La_2]$ to $[FLa_2\square_2]$, whereas the CN decreases. Again, the influence of M–F distances on the ^{19}F δ_{iso} values is emphasized. The absence of two Li^+ ions in $[FLa_2\square_2]$ relative to $[FLi_2La_2]$ is counterbalanced by the decrease in the F–La distance, in agreement with the decrease in the CN. The fluoride ions are therefore brought closer to the La^{3+} corners, which leads to shorter La–F distances (Figure 9).

As already mentioned, the $\delta_{iso}(1)$, $\delta_{iso}(2)$ and $\delta_{iso}(3)$ values increase with x (Figure 5 and Table 5). This means that, for the corresponding environments, the Li–F and/or La–F distances decrease, whereas the cell parameter (Table 1 and Figure 1) and consequently the average distance between the 8b and 16d sites (special positions) increase. Thus, only fluoride ion shiftings toward the occupied corners of the $[FLi_nLa_m\square_{4-n-m}]$ tetrahedra explain the decrease in the Li–F and/or La–F distances. The increase in the $\delta_{iso}(1)$, $\delta_{iso}(2)$ and $\delta_{iso}(3)$ values is related to the increasing amount of vacancies. When x increases, the content of $[FLi_nLa_m\square_{4-n-m}]$ tetrahedra with at least one vacancy, i.e. those involving one or two corners that are not connected, increases: the higher the content of vacancies, the easier the displacement of F^- ions closer to the occupied corners and the shorter the Li–F and/or La–F distances (Figure 9). Indeed, one can notice that the δ_{iso} value increase is higher (δ =8 ppm) for the environments that have a vacancy, i.e.

$[FLi_3\square]$ and $[FLi_2La\square]$ (Table 5). Nevertheless, the $\delta_{iso}(2)$ value also increases, while the corresponding line is assigned to the $[FLi_3La]$ environment. This shows that the Li^+ and La^{3+} displacements, toward the $F^–$ ion, are induced by $F^–$ ion shifts in neighbouring $[FLi_nLa_m\square_{4–n–m}]$ tetrahedra. Such a discussion about the $\delta_{iso}(4)$ and $\delta_{iso}(5)$ values seems to be risky since $[FLiLa_2\square]$ environments are likely to occur. A part of both lines 4 and 5 are then assigned to $[FLiLa_2\square]$ environments. So, $\delta_{iso}(4)$ and $\delta_{iso}(5)$ values cannot strictly be assigned to $[FLi_2La_2]$ and $[FLa_2\square_2]$ environments. Nevertheless the stability of the $\delta_{iso}(4)$ values is not surprising since the $[FLi_2La_2]$ environment is the bulkiest one. Li^+ and La^{3+} displacements, toward the $F^–$ ion, could then be ruled out from steric and electrostatic points of view.

For the $Li_{2–x}La_{(1+x)/3}\square_{(2x–1)/3}Nb_2O_6F$ series, the relative intensities of each ^{19}F NMR line are a bit different. The agreement between the numbers of Li^+, La^{3+} and vacancy per formula deduced from the relative intensities of the ^{19}F NMR lines and the nominal chemical composition (Table 6) remains satisfying. One can remark that the agreement could be improved, for x = 0.9 and x = 1.0, by assuming the occurrence of $[FLiLa_2\square]$ environments as in the $Li_{2–x}La_{(1+x)/3}\square_{(2x–1)/3}Ta_2O_6F$ series. In this case, the relative intensities of lines 4 should be more reduced than those of lines 5, which leads to smaller contents of Li^+ ions and higher contents of vacancies. On the other hand, the $\delta_{iso}(1)$ values in $Li_{2–x}La_{(1+x)/3}\square_{(2x–1)/3}Nb_2O_6F$ do not evolve with x and remain very close to the ^{19}F δ_{iso} value in LiF (–204 ppm[10]). The occurrence of a LiF impurity cannot then be ruled out in the $Li_{2–x}La_{(1+x)/3}\square_{(2x–1)/3}Nb_2O_6F$ compounds. As the intensities of the lines 1 range from 0.7 to 2.1% and as Li and F are both light elements, a LiF impurity is difficult to detect by powder XRD for such contents. One should note that if line 1 is assigned to a LiF impurity, the environment $[FLi_3\square]$ (or $[FLi_4]$) is absent, which confirms the instability of this environment. The occurrence of a LaF_3 impurity seems difficult to establish since the three ^{19}F NMR lines of LaF_3 (–23 to 18 ppm[11,12]) and lines 4 and 5 (Table 6 and Figure 6) overlap. However, if this impurity is present, the relative intensities of lines 4 and 5 are overestimated since these lines are superimposed to the ^{19}F NMR lines of LaF_3. The discrepancy between the relative intensities of each ^{19}F NMR line of the $Li_{2–x}La_{(1+x)/3}$-

Table 8. Values of the R_A, $R_{A'}$, R_B, $R_{B'}$ ionic radii [Å],[a] values of the $(aR_A+a'R_{A'})/(bR_B+b'R_{B'})$ ratio and the crystal structures of the oxyfluorides $A_aA'_{a'}B_bB'_{b'}O_6F$.

Compound	R_A	$R_{A'}$	R_B	$R_{B'}$	$\frac{aR_A+a'R_{A'}}{bR_B+b'R_{B'}}$	Structure	ICSD[b]
$Bi\square Ta_2O_6F$[c]	1.17		0.64		0.91	pyrochlore	25553
β-$Ca_{1.5}\square_{0.5}Nb_2O_6F$[d]	1.12		0.64		1.31	pyrochlore	157314
β-$Ca_{1.5}\square_{0.5}Ta_2O_6F$[d]	1.12		0.64		1.31	pyrochlore	157316
$Li_{1.00}La_{0.67}\square_{0.33}Ta_2O_6F$[e]	0.92	1.16	0.64		1.33	pyrochlore	
$Li_{1.25}La_{0.58}\square_{0.17}Nb_2O_6F$[e]	0.92	1.16	0.64		1.42	pyrochlore	
$LiCaNb_2O_6F$[d]	0.92	1.12	0.64		1.59	pyrochlore	
$LiCaTa_2O_6F$[d]	0.92	1.12	0.64		1.59	pyrochlore	157317
$LiSrNb_2O_6F$[f]	0.92	1.26	0.64		1.70	pyrochlore	92868
$LiSrTa_2O_6F$[g]	0.92	1.26	0.64		1.70	pyrochlore	16185
$Ca_2Nb_2O_6F$[h]	1.12		0.64	0.68	1.70	pyrochlore	63189
$Ca_2Ta_2O_6F$[i]	1.12		0.64	0.68	1.70	pyrochlore	50048
$CdYbTi_2O_6F$[j]	1.10	0.985	0.605		1.72	pyrochlore	108956
$NaYbTiNbO_6F$[j]	1.18	0.985	0.605	0.64	1.74	pyrochlore	108951
$CdYTi_2O_6F$[j]	1.10	1.019	0.605		1.75	pyrochlore	108952
$NaYTiNbO_6F$[j]	1.18	1.019	0.605	0.64	1.77	pyrochlore	108945
$CdGdTi_2O_6F$[j]	1.10	1.053	0.605		1.78	pyrochlore	108955
$CdEuTi_2O_6F$[j]	1.10	1.066	0.605		1.79	pyrochlore	108954
$NaGdTiNbO_6F$[j]	1.18	1.053	0.605	0.64	1.79	pyrochlore	108950
$NaCaNb_2O_6F$[k]	1.18	1.12	0.64		1.80	pyrochlore	24445
$NaEuTiNbO_6F$[j]	1.18	1.066	0.605	0.64	1.80	pyrochlore	108949
$CdNdTi_2O_6F$[j]	1.10	1.109	0.605		1.83	pyrochlore	108953
$NaNdTiNbO_6F$[j]	1.18	1.109	0.605	0.64	1.84	pyrochlore	108948
$NaPrTiNbO_6F$[j]	1.18	1.126	0.605	0.64	1.85	pyrochlore	108947
$NaCeTiNbO_6F$[j]	1.18	1.143	0.605	0.64	1.87	pyrochlore	108946
$NaSrNb_2O_6F$[f]	1.18	1.26	0.64		1.91	pyrochlore	
$NaPbNb_2O_6F$[l]	1.18	1.29	0.64		1.93	pyrochlore	
$KCaNb_2O_6F$[m]	1.51	1.12	0.64		2.05	pyrochlore	240958
$RbCaNb_2O_6F$[n]	1.61	1.12	0.64		2.13	perovskite	
$KSrNb_2O_6F$[o]	1.51	1.26	0.64		2.16	perovskite	249327
$RbNdTiNbO_6F$[p]	1.61	1.109	0.605	0.64	2.18	perovskite	95508
$KPbNb_2O_6F$[l]	1.51	1.29	0.64		2.19	pyrochlore	
$RbPrTiNbO_6F$[p]	1.61	1.126	0.605	0.64	2.20	perovskite	95507
$RbLaTiNbO_6F$[p]	1.61	1.16	0.605	0.64	2.22	perovskite	95506
$RbSrNb_2O_6F$[f]	1.61	1.26	0.64		2.24	perovskite	92867

[a] Ref.[7] [b] Ref.[19] [c] Ref.[24] [d] Ref.[2] [e] This work. [f] Ref.[20] [g] Ref.[25] [h] Ref.[26] [i] Ref.[27] [j] Ref.[22] [k] Ref.[28] [l] Ref.[23] [m] Ref.[29] [n] Ref.[5] [o] Ref.[30] [p] Ref.[21]

$\square_{(2x-1)/3}Ta_2O_6F$ and $Li_{2-x}La_{(1+x)/3}\square_{(2x-1)/3}Nb_2O_6F$ compounds could therefore tentatively be explained by an incomplete reaction for the $Li_{2-x}La_{(1+x)/3}\square_{(2x-1)/3}Nb_2O_6F$ series, which leads to samples with compositions slightly different from those expected. This lower reactivity is corroborated by the narrower domain for the occurrence of the $Li_{2-x}La_{(1+x)/3}\square_{(2x-1)/3}Nb_2O_6F$ solid solution.

Stability of the Oxyfluoride Pyrochlores $A_aA'_{a'}B_bB'_{b'}O_6F$

Subramanian et al.[4] have shown, for the $A_2B_2O_7$ stoichiometry, that the competition between the pyrochlore and the layered perovskite structures is driven by the ratio of the ionic radius R_A/R_B and that pyrochlores can form for $R_{A^{3+}}/R_{B^{4+}}$ up to 2.3 and $R_{A^{2+}}/R_{B^{5+}}$ up to 2.2. As oxide and fluoride ions have similar ionic radii, this analysis has been extended to $A_2B_2O_6F$ oxyfluorides, and a limit for the ratio of the radius of 2.1 was evidenced. For higher values, the $A_2B_2O_6F$ compounds have a layered perovskite structure.[2,5]

Among the 34 oxyfluoride compounds with the formulation $A_aA'_{a'}B_bB'_{b'}O_6F$ (A = alkali metal, alkaline earth metal, Cd, Bi; A′ = alkaline earth metal, rare earth, Y, Pb; B, B′ = Ti, Nb, Ta) reported in the inorganic crystal structure database,[19] in the literature,[5,2,20,21–30] and in this work, 28 adopt the pyrochlore structure and 6 adopt the layered perovskite structure. For each one, we have calculated the $(aR_A+a'R_{A'})/(bR_B+b'R_{B'})$ ratio where R_A, $R_{A'}$, R_B and $R_{B'}$ are the ionic radii of A, A′, B and B′, respectively. This ratio allows for the taking into account of the occurrence of different cations in different proportions and/or vacancies on the same crystallographic site as, for instance, in $Li_{2-x}La_{(1+x)/3}\square_{(2x-1)/3}B_2O_6F$. The $A_aA'_{a'}B_bB'_{b'}O_6F$ compounds are reported in Table 8 by increasing order of the ratio $(aR_A+a'R_{A'})/(bR_B+b'R_{B'})$ values. From these data, it is clear that this ratio governs the stability of the $A_aA'_{a'}B_bB'_{b'}O_6F$ compounds as the R_A/R_B ratio governs the stability of the pyrochlore type $A_2B_2O_7$ compounds.[4] Choy et al.[20] synthesized ion-conducting oxyfluorides $ASrNb_2O_6F$ (A = Li, Na), which presents a Dion–Jacobson layered perovskite structure, by an ion-exchange reaction on the precursor $RbSrNb_2O_6F$. These layered perovskite phases are found to transform, by a hydrolysis process, into the $ASrNb_2O_{6.5}$ defective pyrochlore compounds by heating in air at 540 and 600 °C, respectively;[5] by contrast, if the $ASrNb_2O_6F$ layered perovskite phases are heated at 600 °C in gold sealed tubes filled with N_2 gas, the pyrochlore oxyfluoride phases $ASrNb_2O_6F$ are formed with minor impurities. These facts illustrate, for the $ASrNb_2O_6F$ stoichiometry, the competing situation that exists between the two-dimensional layered perovskite structure and the three-dimensional pyrochlore structure when A = Li or Na; in this case, the pyrochlore form is found to be thermodynamically stable, in agreement with ratio values equal to 1.70 and 1.91, respectively (Table 8). Nevertheless, the ratio value limit of 2.1,[5,2] above which the layered perovskite structure is supposed to be thermodynamically stable, has to be reconsidered since $KPbNb_2O_6F$[23] presents a pyrochlore structure with 2.19 as ratio. Kim et al.[23] propound that the electronic structure of Pb^{2+} affects the structural stability of $KPbNb_2O_6F$, but its assumed role is not explained. From the data gathered in Table 8, it can be concluded that a competition really occurs between the pyrochlore and perovskite structures for ratios ranging from 2.1 to 2.2 for the $A_aA'_{a'}B_bB'_{b'}O_6F$ compounds. Below ratio values of 2.1, the pyrochlore structure is thermodynamically stable. The title compounds, which always present a ratio below 2.1 whatever the x values, fulfill this rule.

Conclusions

Two new oxyfluoride solid solutions $Li_{2-x}La_{(1+x)/3}\square_{(2x-1)/3}B_2O_6F$ (B = Ta, Nb) have been evidenced with composition domains corresponding to $0.6 \le x \le 1.1$ for the Ta compounds and $0.7 \le x \le 1.0$ for the Nb compounds. The compounds adopt the cubic pyrochlore structural type: SG $Fd\bar{3}m$, $Z = 8$ and $a \approx 10.448$ Å. The solid solution limits have been determined from powder samples by XRD measurements. For the two solid solutions, we observe a continuous increase in the cell parameter as x increases. The structural study has been performed by XRD on two single crystals for the Ta and Nb materials. For both, the classical $[B_2O_6F]^{3-}$ network is preserved in which the F^- and O^{2-} ions are strictly ordered on the 8b and 48f sites, respectively, while La^{3+}, Li^+ and the vacancies statistically occupy the 16d site inside the hexagonal tunnels. This average structural description was supplemented by HREM and ^{19}F solid-state NMR techniques with the aim of defining the local structure. If the HREM study reveals significant population fluctuations in the 16d site, the ^{19}F solid-state NMR study allows for the specification of the fluoride ion environments. Five distinct ^{19}F resonances have been observed whose δ_{iso} values are approximately equal for $Li_{2-x}La_{(1+x)/3}\square_{(2x-1)/3}Ta_2O_6F$ and $Li_{2-x}La_{(1+x)/3}\square_{(2x-1)/3}Nb_2O_6F$, which confirms that the fluoride ions are located exclusively on the 8b site. On the basis of the qualitative analysis of their isotropic chemical shifts with the superposition model proposed by B. Bureau et al.[14] as well as of their relative intensities, the five ^{19}F NMR lines were assigned to six different environments for the fluoride ion – $[FLi_3\square]$ (or $[FLi_4]$), $[FLi_3La]$, $[FLi_2La\square]$, $[FLi_2La_2]$, $[FLiLa_2\square]$ and $[FLa_2\square_2]$ – whereas fifteen different environments are expected if a random distribution of Li^+, La^{3+} and $\square$ in the 16d site is assumed. Steric and/or electrostatic constraints explain the absence of environments such as $[FLi\square_3]$, $[FLi_2\square_2]$, $[FLa_3\square]$ and $[FLa_4]$. The low content of $[FLi_3\square]$ (or $[FLi_4]$) proves the low stability of this environment in which the F–Li distances are too short compared to the average distance between the 8b and 16d sites. It has been shown that the La(Li)–F distances decrease with the CN of the F^- ions from the $[FLi_3La]$ to $[FLi_2La\square]$ environments and from the $[FLi_2La_2]$ to $[FLa_2\square_2]$ environments. The fluoride ions located inside the tetahedra that involve vacancies are brought closer to the corners occupied by Li^+ and/or La^{3+}.

These La(Li)–F distances decrease also for the $[FLi_3\square]$ (or $[FLi_4]$), $[FLi_3La]$ and $[FLi_2La\square]$ environments when the average vacancy content increases. The agreement between the number of Li^+, La^{3+} and vacancy per formula deduced from the relative intensities of the ^{19}F NMR lines and the nominal chemical composition is slightly less satisfying for $Li_{2-x}La_{(1+x)/3}\square_{(2x-1)/3}Nb_2O_6F$, but the occurrence of impurities cannot be excluded for these samples. From the identification and the quantification of the $[FLi_nLa_m\square_{4-n-m}]$ environments occurring in these compounds, it can be suggested that the solid solution composition domains are limited, (i) for low x values, i.e. for high Li^+ ion content, by the low stability of the environments $[FLi_3\square]$ (or $[FLi_4]$), (ii) for high x values, i.e. high content of La^{3+} ions and $\square$, by the steric constraints resulting from the large La^{3+} ions and the vacancies.

This work demonstrates again the complementarity of XRD and ^{19}F MAS NMR spectroscopy for the structural characterization of oxyfluoride compounds. It confirms that ^{19}F MAS NMR investigations are very efficient at determining the local environments of fluoride ions, especially when they are surrounded by vacancies and/or different cations occupying the same crystallographic site.

Experimental Section

Synthesis: All the products were obtained from dry La_2O_3 (Johnson Mattey, purity > 99.99%, preheated to 1000 °C for 12 h), B_2O_5 (B = Nb, Ta; Johnson Mattey, purity > 99.85%), Li_2CO_3 (Aldrich, purity > 99.99%), LiF (Aldrich, purity > 99.9%), LaF_3 (Johnson Mattey, purity > 99.99%) and BO_2F, which is prepared by the method described by Frevel and Rinn.[31]

Powder samples of $Li_{2-x}La_{(1+x)/3}\square_{(2x-1)/3}B_2O_6F$ were synthesized from $Li_{0.5}La_{0.5}B_2O_6$, LiF and LaF_3. $Li_{0.5}La_{0.5}B_2O_6$ was first prepared from a mixture of Li_2CO_3, La_2O_3 and B_2O_5 preheated at 550 °C over 6 h and heated at 1100 °C for 4 h in the case of B = Nb or at 1450 °C for 6 h for B = Ta. The fluorides LiF and LaF_3 were added in stoichiometric proportions to $Li_{0.5}La_{0.5}B_2O_6$ in a glove box under an anhydrous atmosphere. The mixture was then placed in a platinum tube and outgassed overnight at 150 °C under vacuum, sealed under an N_2 atmosphere and heated over 6 h at 1000 °C for the Nb materials and at 1200 °C for the Ta compounds. The continuous evolution of the cell parameters as well as the purity of the samples revealed by the XRD patterns allow for the retaining of the nominal value as the sample chemical composition.

For the structural determination, single crystals were prepared by first mixing La_2O_3, Li_2CO_3 and B_2O_5 in the stoichiometry $Li_{1.5}La_{0.5}B_2O_6F$. After grinding, the mixture was heated at 850 °C. BO_2F was then added, and the mixture, thoroughly ground, introduced in a platinum tube, which was heated under vacuum at 150 °C over 10 h. This tube was finally sealed under a N_2 atmosphere. For the tantalum compound, the Pt tube was heated at 1500 °C for 10 min in order to melt the solids and then slowly cooled down to 900 °C over 6 d. In this way, we obtained small colourless octahedral crystals. For the niobium compound, the melting temperature (1250 °C) was maintained over 30 min, and the cooling rate corresponded to 50 °C/d. Similar small colourless octahedral crystals were also obtained.

Table 9. Crystallographic parameters and operating conditions of the X-ray data collection and of the refinement for $Li_{1.00}La_{0.67}\square_{0.33}Ta_2O_6F$ and $Li_{1.25}La_{0.58}\square_{0.17}Nb_2O_6F$.

	$Li_{1.00}La_{0.67}\square_{0.33}Ta_2O_6F$	$Li_{1.25}La_{0.58}\square_{0.17}Nb_2O_6F$
Symmetry	cubic	cubic
Space group	$Fd\bar{3}m$ (No. 227)	$Fd\bar{3}m$ (No. 227)
$a = b = c$ [Å]	10.448(1)	10.448(7)
V [Å^3]	1140.51	1140.51
Z	8	8
Formula weight [g mol^{-1}]	576.37	390.05
$d_{calcd.}$ [g cm^{-3}]	6.70	4.43
Temperature [°C]	20	20
Radiation	Mo-K_α (graphite monochromatized)	Mo-K_α (graphite monochromatized)
Crystal volume [10^{-4} mm^3]	33.80	22.16
Scanning mode	$\omega/2\theta$	$\omega/2\theta$
Aperture [mm]	4 × 4	4 × 4
Range registered:		
2θ max [°]	89.97	74.95
h, k, l max	20, 13, 17	11, 12, 17
Absorption coefficient [mm^{-1}]	$\mu = 43.15$	$\mu = 7.51$
Absorption correction	Gaussian method	Gaussian method
T_{max}, T_{min}	0.010, 0.098	0.406, 0.614
R_{int}	0.0436	0.0420
Secondary extinction coefficient	0.0052(7)	0.0035(5)
Total reflections measured	273	872
Independent reflections measured, used in refinement	231	170
Number of refined parameters	11	11
Weighting scheme, w	$\frac{1}{\sigma^2(F_o^2) + (0.10P)^2}$[a]	$\frac{1}{\sigma^2(F_o^2) + (0.0558P)^2 + 13.73P}$[a]
max, min [e$^-$Å^{-3}]	3.63, –3.45	0.65, –0.90
R_1 for data with $F_o > 4\sigma(F_o)$, for all data	0.0447, 0.0557	0.0247, 0.0287
wR_2	0.1205	0.0792

[a] $P = [\max(F_o^2,0)+2F_c^2]/3$.

Characterization: The powder XRD patterns were recorded at room temperature with a PANalytical X'pert Pro diffractometer equipped with the X'Celerator detector by using monochromated Cu-K_α radiation. The data were collected in the 5–130° 2θ range with a 0.017° step and 210 s per step. The structure refinements were carried out by the Rietveld method,[32] by using the Fullprof[6] profile refinement program (Pseudo Voigt function).

For both compounds, the single-crystal X-ray data collection was performed with a Siemens AED2 four-circle diffractometer with a $\omega/2\theta$ mode. The absorption correction was made with the SHELX-76 program,[33] while structure refinements were performed with the SHELX-93 software.[34] The relevant crystallographic parameters and further details of the X-ray data collections and of the refinements are summarized in Table 9. Further details on the crystal structure investigations may be obtained from the Fachinformationszentrum Karlsruhe, 76344 Eggenstein-Leopoldshafen, Germany (Fax: +49-7247-808-666; E-mail: crysdata@fiz-karlsruhe.de), on quoting the depository numbers CSD-421959 and –421960 for $Li_{1.00}La_{0.67}\square_{0.33}Ta_2O_6F$ and $Li_{1.25}La_{0.58}\square_{0.17}Nb_2O_6F$, respectively.

The TEM study (SAED and HREM) was performed with a JEOL 2010 electron microscope, operating at 200 kV and equipped with a side-entry ±30° double tilt specimen holder. Small crystals were crushed and ultrasonically dispersed in *n*-butanol, and one drop of this suspension was placed on a holey carbon film Cu grid, in order to support a random orientation of the crystallites after evaporation. The EMS program package[35] was used to calculate simulated images for different thickness and defocus values with the following parameters: spherical aberration constant Cs = 1.0 mm, defocus spread Δ = 12 nm, illumination semi-angle α = 0.8 mrad, objective lens aperture diameter 11.6 nm^{-1}.

The solid-state NMR experiments were performed with an Avance 300 Bruker spectrometer (magnetic field of 7 T) operating, for ^{19}F, at a Larmor frequency of 282.2 MHz. ^{19}F MAS NMR spectra were recorded by using a ^{19}F/X probe head with a 2.5 mm diameter ZrO_2 rotor and by employing the Hahn echo sequence. The ^{19}F Hahn-echo spectra were acquired in 256 scans, by using a 2.7-µs 90° pulse and an interpulse delay synchronized with the rotor period. The recycle delay was taken to 5 s. The ^{19}F chemical shifts were referenced to $CFCl_3$. The discrimination of isotropic peaks from spinning sidebands was achieved by recording spectra at different spinning frequencies. The reconstruction of the ^{19}F NMR spectra were performed with the DMFIT software,[36] including spinning sidebands, by using six adjustable parameters: isotropic chemical shift δ_{iso}, chemical shift anisotropy δ_{aniso}, chemical shift asymmetry parameter η, line width, relative line intensity and line shape. In this study, the δ_{iso} values, the relative intensities and the line widths are the relevant parameters; the other parameters are not discussed at all.

Supporting Information (see footnote on the first page of this article): Experimental and calculated X-ray powder patterns of $Li_{1.1}La_{0.63}\square_{0.27}Nb_2O_6F$; experimental and calculated ^{19}F MAS spectra of $Li_{2-x}La_{(1+x)/3}\square_{(2x-1)/3}Ta_2O_6F$ (x = 0.7 and 0.9) and $Li_{2-x}La_{(1+x)/3}\square_{(2x-1)/3}Nb_2O_6F$ (x = 0.7, 0.8, 0.9 and 1.0).

---

[1] A. F. Wells, *Structural Inorganic Chemistry*, 5th ed., Clarendon Press, Oxford, **1987**.
[2] F. Le Berre, M.-P. Crosnier-Lopez, C. Galven, J.-L. Fourquet, C. Legein, M. Body, J.-Y. Buzaré, *Dalton Trans.* **2007**, 2457–2466.
[3] L. Sronek, J. Lhoste, M. Gaudon, C. Legein, J.-Y. Buzaré, M. Body, G. Crinière, A. Tressaud, S. Pechev, A. Demourgues, *J. Phys. Chem. C* **2008**, *112*, 860–866.
[4] M. A. Subramanian, G. Aravamudan, G. V. Subba Rao, *Prog. Solid State Chem.* **1983**, *15*, 55–143.
[5] J.-Y. Kim, I. Chung, S.-J. Kim, J.-H. Choy, *J. Mater. Chem.* **2002**, *12*, 1001–1004.
[6] J. Rodriguez-Carvajal, *Program FULLPROF*, version July **2008**.
[7] R. D. Shannon, *Acta Crystallogr., Sect. A* **1976**, *32*, 751–767.
[8] N. E. Brese, M. O'Keeffe, *Acta Crystallogr., Sect. B* **1991**, *47*, 192–197.
[9] A. Zalkin, D. H. Templeton, *Acta Crystallogr., Sect. B* **1985**, *41*, 91–93.
[10] J. M. Miller, *Prog. Nucl. Magn. Reson. Spectrosc.* **1996**, *28*, 255–291.
[11] F. Wang, C. P. Grey, *Chem. Mater.* **1997**, *9*, 1068–1070.
[12] J. F. Stebbins, Q. Zeng, *J. Non-Cryst. Solids* **2000**, *262*, 1–5.
[13] J. Thewlis, *Acta Crystallogr.* **1955**, *8*, 36–38.
[14] B. Bureau, G. Silly, J. Emery, J.-Y. Buzaré, *Chem. Phys.* **1999**, *249*, 89–104.
[15] M. Body, G. Silly, C. Legein, J.-Y. Buzaré, *Inorg. Chem.* **2004**, *43*, 2474–2485.
[16] G. Silly, M. Body, J.-Y. Buzaré, C. Legein, B. Bureau, *C. R. Chim.* **2004**, *7*, 403–416.
[17] C. Martineau, M. Body, C. Legein, G. Silly, J.-Y. Buzaré, F. Fayon, *Inorg. Chem.* **2006**, *45*, 10215–10223.
[18] C. Legein, F. Fayon, C. Martineau, M. Body, J.-Y. Buzaré, D. Massiot, E. Durand, A. Tressaud, A. Demourgues, O. Péron, B. Boulard, *Inorg. Chem.* **2006**, *45*, 10636–10641.
[19] *Inorganic Crystal Structure Database (ICSD)*, version 1.4.6; FIZ Karlsruhe and NIST: Germany and Maryland, **2009**.
[20] J.-H. Choy, J.-Y. Kim, S.-J. Kim, J.-S. Sohn, *Chem. Mater.* **2001**, *13*, 906–912.
[21] G. Caruntu, L. Spinu, J. B. Wiley, *Mater. Res. Bull.* **2002**, *37*, 133–140.
[22] J. Grannec, H. Baudry, J. Ravez, J. Portier, *J. Solid State Chem.* **1974**, *10*, 66–71.
[23] S. C. Kim, J. K. Kang, S. J. Kim, *Bull. Korean Chem. Soc.* **2010**, *31*, 497–499.
[24] K. Dihlstroem, A. Westgren, *Z. Anorg. Allg. Chem.* **1937**, *235*, 153–160.
[25] A. G. Tutov, V. I. Bader, I. E. Myl'nikova, *Kristallografiya* **1972**, *17*, 406–407.
[26] Q. B. Yang, S. Andersson, *Acta Crystallogr., Sect. B* **1987**, *43*, 1–14.
[27] T. Siegrist, R. J. Cava, J. J. Krajewski, *Mater. Res. Bull.* **1997**, *32*, 881–887.
[28] H. R. von Gaertner, *Neues Jahrbuch fuer Mineralogie, Geologie und Palaeontologie. Beilagen, Abt. A* **1930**, *61*, 1–30.
[29] C.-Y. Yoo, S.-J. Kim, *Acta Crystallogr., Sect. E* **2007**, *63*, i203–i204.
[30] C.-Y. Yoo, K.-P. Hong, S.-J. Kim, *Acta Crystallogr., Sect. C* **2007**, *63*, i63–i65.
[31] L. K. Frevel, H. W. Rinn, *Acta Crystallogr.* **1956**, *9*, 626–627.
[32] H. M. Rietveld, *J. Appl. Crystallogr.* **1969**, *2*, 65–71.
[33] G. M. Sheldrick, *SHELX-76: Program for Crystal Structure Determination*, University of Cambridge, **1976**.
[34] G. M. Sheldrick, *SHELX-93: A Program for the Refinement of Crystal Structures for Diffraction Data*, University of Göttingen, Germany **1993**.
[35] P. Stadelman, *Ultramicroscopy* **1987**, *21*, 131.
[36] D. Massiot, F. Fayon, M. Capron, I. King, S. Le Calvé, B. Alonso, J. O. Durand, B. Bujoli, Z. Gan, G. Hoatson, *Magn. Reson. Chem.* **2002**, *40*, 70–76.

Received: May 28, 2010